SANDIA REPORT
SAND2010-7013
Unlimited Release
Printed October 2010

Nanocrystal-enabled Solid State Bonding

Elizabeth A. Holm, Joseph D. Puskar, Mark Reece, Veena Tikare, Cristina Garcia Cardona, Luke N. Brewer

Prepared by
Sandia National Laboratories
Albuquerque, New Mexico 87185 and Livermore, California 94550

Sandia National Laboratories is a multi-program laboratory managed and operated by Sandia Corporation, a wholly owned subsidiary of Lockheed Martin Corporation, for the U.S. Department of Energy's National Nuclear Security Administration under contract DE-AC04-94AL85000.

Issued by Sandia National Laboratories, operated for the United States Department of Energy by Sandia Corporation.

Available to DOE and DOE contractors from
U.S. Department of Energy
Office of Scientific and Technical Information
P.O. Box 62
Oak Ridge, TN 37831

Telephone: (865) 576-8401
Facsimile: (865) 576-5728
E-Mail: reports@adonis.osti.gov
Online ordering: http://www.osti.gov/bridge

Available to the public from
U.S. Department of Commerce
National Technical Information Service
5285 Port Royal Rd.
Springfield, VA 22161

Telephone: (800) 553-6847
Facsimile: (703) 605-6900
E-Mail: orders@ntis.fedworld.gov
Online order: http://www.ntis.gov/help/ordermethods.asp?loc=7-4-0#online

SAND2010-7013
Unlimited Release
Printed October 2010

Nanocrystal-enabled Solid State Bonding

Elizabeth A. Holm[1], Joseph D. Puskar[2], Mark Reece[3], Veena Tikare[4]
[1]Computational Materials Science and Engineering;
[2]Materials Characterization;
[3]Multiscale Metallurgical Science and Technology
[4]Advanced Nuclear Fuel Cycle Technology
Sandia National Laboratories
P.O. Box 5800
Albuquerque, New Mexico 87185 U.S.A.

Cristina Garcia Cardona
San Diego State University
San Diego, CA 92182-1245 U.S.A.

Luke N. Brewer
Naval Postgraduate School
Monterey, CA 93943-5019 U.S.A.

Abstract

In this project, we performed a preliminary set of sintering experiments to examine nanocrystal-enabled diffusion bonding (NEDB) in Ag-on-Ag and Cu-on-Cu using Ag nanoparticles. The experimental test matrix included the effects of material system, temperature, pressure, and particle size. The nanoparticle compacts were bonded between plates using a customized hot press, tested in shear, and examined post mortem using microscopy techniques. NEDB was found to be a feasible mechanism for low-temperature, low-pressure, solid-state bonding of like materials, creating bonded interfaces that were able to support substantial loads. The maximum supported shear strength varied substantially within sample cohorts due to variation in bonded area; however, systematic variation with fabrication conditions was also observed. Mesoscale sintering simulations were performed in order to understand whether sintering models can aid in understanding the NEDB process. A pressure-assisted sintering model was incorporated into the SPPARKS kinetic Monte Carlo sintering code. Results reproduce most of the qualitative behavior observed in experiments, indicating that simulation can augment experiments during the development of the NEDB process. Because NEDB offers a promising route to low-temperature, low-pressure, solid-state bonding, we recommend further research and development with a goal of devising new NEDB bonding processes to support Sandia's customers.

Acknowledgements

This work was supported by an FY10 Late Start Laboratory Directed Research and Development (LDRD) project. Sandia is a multiprogram laboratory operated by Sandia Corporation, a Lockheed Martin Company, for the United States Department of Energy's National Nuclear Security Administration under Contract No. DE-AC04-94AL85000.

Table of Contents

List of Figures

List of Tables

1. Project Summary

1.1 Introduction

Virtually all engineered components are comprised of materials that have been joined together. While joining technology has advanced, there are still critical applications where the joining solutions create unacceptable problems such as thermal stress-induced cracking, phase transformations, and thermal component damage. These problems are exacerbated by joining dissimilar materials or complex shapes and by bonding processes that occur late in assembly.

Many of these problems occur because bonding temperatures and pressures are quite high. For example, welding and brazing use solidification of molten materials to form the joint, potentially leading to thermal stress generation and profound microstructural changes. Solid-state diffusion bonding requires extreme tolerances on the joined surfaces, high temperatures for interdiffusion, and fairly simple geometries for pressure application. Because of these limitations, customers within DOE (NW, ERN) and at other agencies (DSA) would welcome new low temperature, low pressure bonding processes.

The use of nanocrystalline metals as diffusion bonding materials can potentially solve some of these crucial joining problems. The large, stored energy content, high surface area, and short diffusion distances in nanocrystalline materials could drive the diffusion bonding process to much lower temperatures and pressures than traditional approaches. Recent work in Japan [1-3] has demonstrated this approach using silver nanoparticles to bond copper substrates at very low temperatures (300°C) and pressures (1-5MPa). Although this concept is very promising, it is unclear how to explain or predict this phenomenon.

The goals of this proof-of-principle study were: 1.) to determine the feasibility of the nanocrystal-enabled diffusion bonding (NEDB) approach; 2.) to evaluate the applicability of sintering theory and simulation to NEDB; and 3.) to begin to explore the NEDB parameter space.

1.2 Results

In this project, we performed a preliminary set of sintering experiments to examine nanocrystal-enabled diffusion bonding in like materials (Ag-on-Ag and Cu-on-Cu) using Ag nanoparticles. The experimental test matrix included the effects of material system, temperature, pressure, and particle size. The nanoparticle compacts were bonded between plates using a customized hot press. After bonding, the plates were tested in shear, and the bonded area was examined post mortem using microscopy techniques. NEDB was successful in creating bonded interfaces that were able to support substantial loads. The maximum supported shear strength varied substantially within sample cohorts due to variation in bonded area; however, systematic variation with fabrication conditions was also observed.

A complementary suite of mesoscale sintering simulations was performed in order to understand whether sintering models can aid in understanding the NEDB process. A pressure-assisted sintering model was incorporated into the SPPARKS kinetic Monte Carlo sintering code. Two particle sizes and two applied pressures were simulated. Both increased pressure and decreased particle size aid in sintering, as observed experimentally for NEDB. In addition, deformation of the particle compact is predicted. These results indicated that simulation can augment experiments during the development of the NEDB process.

1.3 Conclusions

1. Nanocrystal-enabled diffusion bonding (NEDB) is a feasible mechanism for low-temperature, low-pressure, solid-state bonding of like materials.

2. Sintering theory and simulation provide a useful complement to experiment in the development of the NEDB process.

3. A preliminary exploration of parameter space suggests the potential for NEDB process optimization in temperature, pressure, and particle size space.

4. Because NEDB offers a promising route to low-temperature, low-pressure, solid-state bonding, we recommend further research and development with a goal of devising new NEDB bonding processes to support Sandia's customers.

1.4 References for Section 1

1. Akada, Y., et al., *Interfacial bonding mechanism using silver metallo-organic nanoparticles to bulk metals and observation of sintering behavior*. Mater. Trans., 2008. **49**(7): p. 1537-1545.
2. Ide, E., et al., *Metal-metal bonding process using Ag metallo-organic nanoparticles*. Acta Mater., 2005. **53**(8): p. 2385-2393.
3. Wakuda, D., K.S. Kim, and K. Suganuma, *Room-Temperature Sintering Process of Ag Nanoparticle Paste*. IEEE Trans. Compon. Packag. Tech., 2009. **32**(3): p. 627-632.

2. Experimental Method and Results

2.1 Sample Fabrication

Previous work was done using Ag nanoparticles and Cu substrates polished to a 1 μm finish [1-3]. These substrates were heated at 1°C/s to 300°C and held under a pressure of 1 MPa or 5 MPa for 300 s. The temperature was selected based on the breakdown temperature of the organic shell on the Ag nanoparticles. Though not mentioned in reference [2], this temperature is also 20°C above the breakdown temperature of Ag_2O in air. Two sizes of Ag particles were considered: 11 nm and 100 nm. Shear strengths of 25 – 40 MPa for the 11 nm particle joints were reported.

For our experiments, we created a test matrix that used the same pressures (1 MPa and 5 MPa) as in reference [2] but varied the material system, temperature, and particle size. Material combinations of similar metals, i.e. Cu-on-Cu or Ag-on-Ag, were constructed from a substrate that was always 9.5 mm in diameter and 3 mm thick. Two different sized disks, of the same material as the substrate, were used in the stack-up depending on the bonding pressure: 6.4 mm diameter for 1 MPa bonding pressure and 4.8 mm diameter for 5 MPa bonding pressure with both disks having a thickness of 3 mm. Two different nanoinks were used, both of which contained silver nanoparticles: UT Ink, which had a 5 to 8 nm silver particle size range and Novacentric Ink which had a 25 nm silver particle size. The inks were applied to the smaller disk in the material combination, either the 4.8 or 6.4 mm diameter disk, depending on the bonding pressure. The inks were printed onto the disks and thought to have a thickness of approximately 2 μm that was reasonably uniform. The inks were mostly dried during the printing process and were fully dry when the disks were assembled into a stack-up which was then bonded under an applied load of 2.23 kg for the 1 MPa samples and 9.079 kg for the 5 MPa samples. The samples were bonded at three temperatures: 300°C, 350°C and 400°C. Four samples at each condition and from each substrate material were run to provide three for testing and one for metallographic sectioning The total number of samples created was 4 samples x 3 temperatures x 2 pressures x 2 particle sizes x 2 materials systems = 96 samples.

Our furnace, a Barnstead Thermolyne 1300, was set up in a fume-hood, which was a requirement given the need to handle the nanoparticles. There was no ability to control the atmosphere of the furnace. The interior of the furnace is 10.2 cm X 10.2 cm X 12.7 cm deep. This limitation, as well as a desire to minimize the thermal mass in contact with the sample, necessitated the use of springs to achieve the force needed. Springs constructed from Inconel X-750 were acquired from Coiling Technologies, Inc, which were heat-treated to exhibit minimal change in compressive force to a temperature of 500°C. Lightweight frames from alloy 17-4 PH stainless steel were constructed, with a copper plug at the bottom to aid in heat-up, as shown in Figures 2.1 and 2.2.

Our furnace was profiled using a type K thermocouple embedded in a copper disc for ballast, as shown in Figure 2.3. Once temperature settings were established, the heating characteristics of the frames were examined using thermocouples embedded in copper buttons machined to the size of a 1 MPa and a 5 MPa sample. The load-frame alone placed in the furnace, which was idling at temperature, required nearly 50 minutes to reach temperature. So 2.5 kg of mild steel

were added to the interior of the furnace to act as thermal ballast, as shown in Figure 2.4. This reduced the heat-up time to 30 minutes; much slower than the original experiments, but as fast as the system could achieve without extensive modifications to the furnace or the fume hood, both of which were beyond the scope of this study.

2.2 Mechanical testing

Shear testing was performed using a custom built device that is typical of that used for performing precision microshear testing. The substrate was held in a recessed opening while a knife edge tool was pressed against the smaller diameter disk. The load was increased until the disks were sheared apart. The load was monitored using a load cell capable of accurately determining small load values with sub-kilogram resolution. All data was electronically captured. Three of the four samples bonded at any given set of conditions were tested while the fourth sample was retained for future metallographic examination.

The results of the shear tests are shown in Table 2.1, which reports the nominal, maximum shear stress supported by each sample before it broke. The stress was calculated by dividing the maximum load by the cross-sectional area of the smaller disk used in the bonded assembly. It was clear looking at the fractured specimens that in most samples, the bonded area is significantly smaller than the full available cross section of the small diameter part, and it varies in both extent and location. While it would seem intuitive that the centermost point of the disk should have demonstrated the greatest degree of bonding, this was actually the exception, not the norm. Some examples of the sheared interface will be presented in the next section.

Because the entire interface was not bonded in the majority of the specimens, the nominal shear stress is not equivalent to the actual stress. Attempts were made to characterize the bonded area fraction, but this turned out to be a non-trivial exercise that grew in scope to an intractable point within the constraints of this project. While it can only be speculated at this point, the lack of full area bonding is likely due to a combination of factors such as how the samples were polished, how the load was applied during the bonding process, how the nanoink was applied, and finally the lack of atmosphere control in the furnace, which will be explored more in the next section. It is reasonable to state that the actual shear stresses were likely appreciably higher given that the actual bonded areas were much smaller than the nominal areas. As an example, sample Cu-Cu 400°C, 5 MPa, UT ink, sample #1 was only bonded over approximately 1/3 of the surface and had a nominal shear stress of 15 MPa. Correcting for the reduced cross-sectional area would suggest an actual shear stress value closer to 45 MPa, which is within the range of reported strength values from previous studies. For the majority of the samples, the maximum load occurred at the time of break, but for some, especially the Ag-on-Ag system at 1 MPa and 400°C, the load curve suggests tearing instead of a clean break.

Although it is not quantitative, the shear stress data nonetheless support some qualitative conclusions. First, it is clear that the NEDB process can result in bonds that can support substantial shear loads in both materials systems studied. This is the first examination of NEDB outside the Ag-on-Cu system, and it confirms NEDB as a viable joining process for various materials systems. Second, the load data indicate systematic variation with processing parameters, including temperature, pressure, and particle size. This suggests that the NEDB

process could be optimized with respect to these parameters in order to achieve higher bond strength.

Table 2.1 Nominal maximum shear stresses supported by NEDB samples. Stress is reported in MPa and was calculated for the nominal diameters of the smaller disks, without correction for the actual bonded area.

UT ink - 5 to 8 nm particle size

Copper to Copper

Temperature	300C		350C		400C	
Joining Pressure	**1MPa**	**5MPa**	**1MPa**	**5MPa**	**1MPa**	**5MPa**
Sample #1	no data	10.0	no data	16.8	6.4	13.3
Sample #2	2.6	7.7	no data	9.3	4.7	15.7
Sample #3	3.0	7.6	3.2	17.9	7.4	15.2

Silver to Silver

Temperature	300C		350C		400C	
Joining Pressure	**1MPa**	**5MPa**	**1MPa**	**5MPa**	**1MPa**	**5MPa**
Sample #1	9.6	9.5	17.0	6.6	5.9	17.0
Sample #2	12.4	22.0	7.6	8.6	6.9	8.9
Sample #3	6.6	15.2	5.6	11.0	8.0	7.5

Novacentric Ink - 25 nm particle size

Copper to Copper

Temperature	300C		350C		400C	
Joining Pressure	**1MPa**	**5MPa**	**1MPa**	**5MPa**	**1MPa**	**5MPa**
Sample #1	1.4	no data	4.1	1.4	2.1	4.8
Sample #2	0.2	no data	4.4	3.4	1.3	no data
Sample #3	2.7	no data	10.0	no data	1.1	no data

Silver to Silver

Temperature	300C		350C		400C	
Joining Pressure	**1MPa**	**5MPa**	**1MPa**	**5MPa**	**1MPa**	**5MPa**
Sample #1	2.6	8.0	9.3	4.1	5.7	15.8
Sample #2	3.6	9.9	5.5	2.9	6.9	15.5
Sample #3	3.7	5.7	11.4	10.0	6.5	12.5

2.3 Fractography and Microstructural Characterization

Macrographs of some sheared samples are shown in Figure 2.5. Both of these images were taken of the smaller disk, onto which the silver nanoink was deposited. For both samples, the bonding

temperature was 400°C; in Figure 2.5(a), the sample was bonded at 5 MPa using the UT ink (Cu-Cu 400°C, 5 MPa, UT ink, sample #1), and the sample in Figure 2.5(b) was bonded at 1 MPa with the 25 nm particle ink (Cu-Cu 400°C, 1 MPa, Novacentric ink, sample #3). Figure 2.5(a) shows a reasonably clear fracture surface that suggests that only a fraction of the total surface area available for bonding was well adhered – the silver area on the upper left region of the disk. Figure 2.5(b) shows a much less clear area of bonding on the fracture surface.

Additional analysis was performed on Cu-Cu 400°C, 5 MPa, UT ink, sample #1. Figure 2.5(a) shows a well-bonded area (upper left corner) that is surrounded by a region of darker gray material that itself is surrounded by a copper colored region. Finally, the remaining area on the disk can be seen to have a reasonably uniform, silver appearance. Fractography was performed on the fracture surfaces of disks using an SEM. Figure 2.6 is an image taken from the center of the well-bonded region of the fracture surface. On both halves of the assembly, i.e. both the large and small copper disks, a similar fracture appearance was observed that consisted of dimple rupture. Fracture within the silver layer suggests that the silver bonded well to the copper substrates, at least in some areas. Dimple rupture is what one would expect from a well consolidated and bonded material.

Figure 2.7 shows a higher magnification image of the copper colored region, with a backscattered electron image [Figure 2.7(a)] and a secondary electron image [Figure 2.7(b)]. The backscattered electron (BSE) image is useful for determining composition and shows the bright regions that are silver and darker regions which are a mixture of copper and oxygen. The compositional distribution is also shown by energy dispersive spectroscopy maps, Figure 2.8. Secondary electron images are very useful for capturing surface topography and taken together with the BSE image reveal some interesting features of the fracture surface, specifically that silver is “behind” a layer of copper and oxygen rich material. Rather than fracturing in the silver region, a layer of the copper-rich material was pulled off of the copper disk. There is no sign of ductile fracture on this surface which would suggest that the sample failed in the copper base metal, but rather it is believed that the fracture is occurring between a copper oxide that is forming during processing and the underlying copper substrate material.

Cross-sectional samples of untested samples were prepared and an example of sample Cu-Cu 350°C, 5 MPa, UT ink is shown in Figure 2.9. While this sample has not been shear tested, it can be seen that the silver layer appears to have bonded to itself, as well as the copper substrates in areas, but overall has multiple points of failure. In addition, a thick copper oxide layer can be seen on both copper substrate surfaces. On the top left of the silver layer, the copper oxide seems to be well bonded to the silver layer and has separated from the copper substrate. Along the bottom of the bonded region, the oxide is generally still bonded to both the substrate and the silver, though not completely. The silver being bonded to the copper oxide which has separated from the copper layer is consistent with the results presented in Figures 2.7 and 2.8 for the shear tested specimens. It is also interesting to observe that the silver layer itself is cracked in the middle of the bond layer and furthermore, appears to have density variations through the thickness. These results for an untested sample suggest that the interpretation of the fracture surfaces is not trivial as substantial damage may exist before any of the actual shear testing has occurred.

While the interpretation of the fracture surfaces is not trivial, several interesting themes were observed. The nanoinks were successful in bonding to some surfaces of the substrates. In some cases, this appeared to be copper oxide while in other cases it was likely to copper that had much less oxide given the high shear strength values as well as the dimple rupture fracture surfaces that were observed. It was also observed that in all cases the actual bonded areas were much less than the full cross-section of the smaller disks. As stated previously, this suggests that the actual load carrying capacity of the bonded material was much higher than the nominal shear stress values that were calculated and presented in Table 2.1. It would stand to reason that future work should focus on keeping the substrate materials oxide free throughout the processing cycle and better distributing the load such that complete bonding can be achieved over the full interface.

A common characteristic of all the specimens that were tested is that the entire interface never bonded. It is believed that the inks were printed in a reasonably uniform method, but this should be examined. The samples planarity may not have been sufficient for samples heated to only 400C with a 2 micron or so layer of silver in-between. Perhaps other methods, such as diamond single point turning, may be better for surface preparation. The method of applying stress should also be examined. While relatively low pressures were studied in this experiment, it might make sense to bond under somewhat higher pressures.

Thick layers of copper oxide were also observed which would not be expected to help bonding in any way. Heating the samples in an environmentally controlled furnace would likely prevent the oxidation of the copper samples. This is complicated by the current procedures required to handle nanoparticles. Individually canning the samples in a vacuum before processing would likely prevent the copper oxidation, as this is often how diffusion bonds are produced using hot isostatic pressing, although what this would specifically look like is not clear at this point. It may also be beneficial to sinter in a reducing atmosphere furnace, though the temperatures involved my not provide any benefit, beyond the displacement of oxygen. Study of the removal of the organic suspension material used in the nanoinks is also recommended.

2.4 Conclusions

1. Ninety-six NEDB samples were fabricated using a customized load frame. The experimental matrix included two materials systems, two nanoparticle sizes, three temperatures, and two bonding pressures.

2. Shear tests were performed on 72 of the samples. NEDB was successful in creating bonded interfaces that were able to support substantial loads.

3. The maximum supported shear load varied substantially within sample cohorts due to variation in bonded area; however, systematic variation with fabrication conditions was also observed.

4. Fractography showed evidence of particle consolidation on the fracture surface. Fracture varied from ductile where the nanoparticles bonded to clean substrate to nonductile where the nanoparticles bonded to a surface oxide layer.

5. Cross-sections of unsheared specimens showed a wealth of features that suggest future studies of the NEDB process, including prevention of substrate oxidation, improvement of substrate planarity, and studies of ink deposition, as well as further examination of temperature, pressure, and particle size.

2.5 References for Section 2

1. Akada, Y., et al., *Interfacial bonding mechanism using silver metallo-organic nanoparticles to bulk metals and observation of sintering behavior*. Mater. Trans., 2008. **49**(7): p. 1537-1545.
2. Ide, E., et al., *Metal-metal bonding process using Ag metallo-organic nanoparticles*. Acta Mater., 2005. **53**(8): p. 2385-2393.
3. Wakuda, D., K.S. Kim, and K. Suganuma, *Room-Temperature Sintering Process of Ag Nanoparticle Paste*. IEEE Trans. Compon. Packag. Tech., 2009. **32**(3): p. 627-632.

2.4 Figures for Section 2

Figure 2.1. Frame, spring and pistons. The oxidized copper base is below the frame.

Figure 2.2. Assembled frames with substrates. The 1MPa frame is on the left, the 5 MPa on the right.

Figure 2.3. Load-frames and ballast set up for profiling furnace.

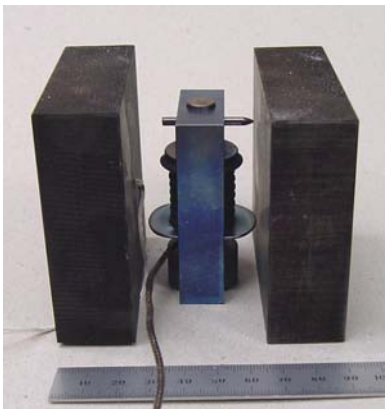

Figure 2.4. Placement of steel ballast and load-frame in furnace.

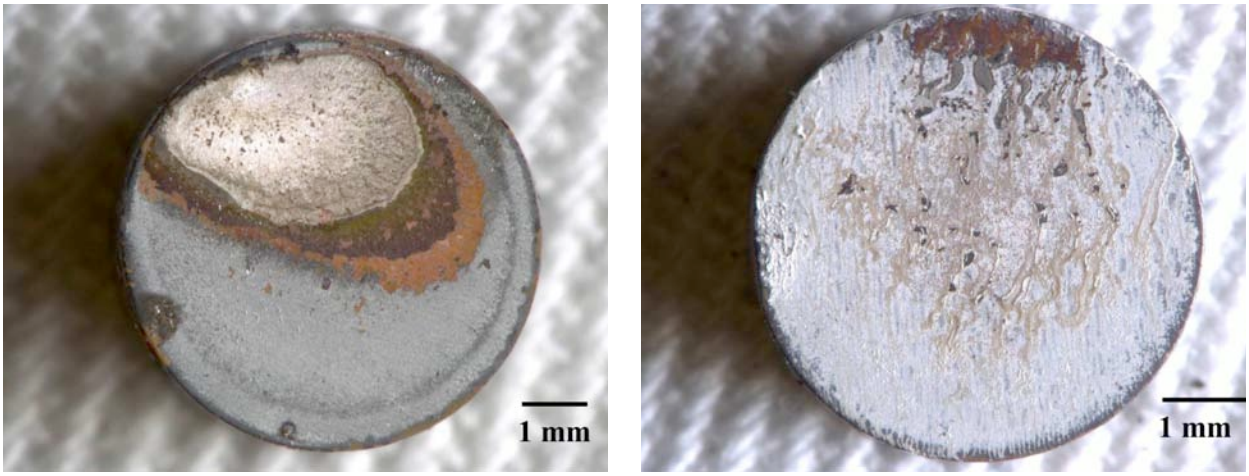

(a) (b)

Figure 2.5. Examples of macro images of fracture surface. (a) Cu-Cu 400°C, 5 MPa, UT ink, sample #1 and (b) Cu-Cu 400°C, 1 MPa, Novacentric ink, sample #3. The bonded area can be seen clearly on the top surface as only a fraction of the total surface area, while the bottom sample bonded area is not as clear.

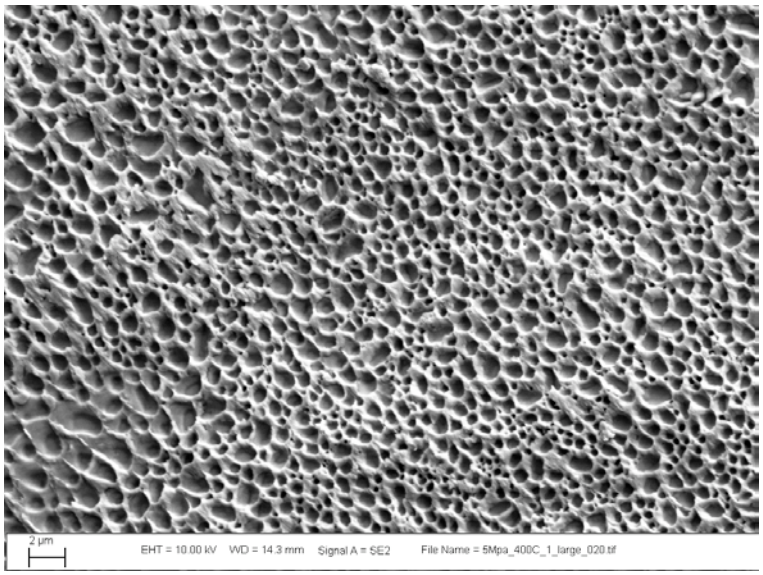

Figure 2.6. Secondary electron image of the well bonded region in Cu-Cu 400°C, 5 MPa, UT ink sample #1. The fracture consists of a classic shear dimple rupture which is what would be expected from a well bonded and consolidated sample.

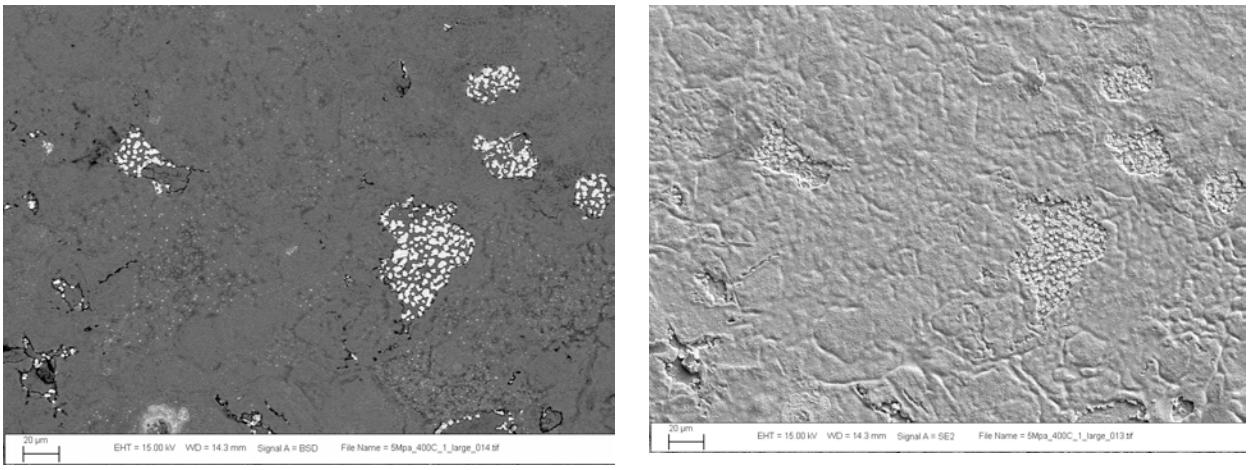

(a) (b)

Figure 2.7. (a) Back-scattered electron and (b) secondary electron images of copper colored region of Cu-Cu 400°C, 5 MPa, UT ink, sample #1. The silver layer is captured below the surface of the fracture suggesting that the failure occurred outside of the silver/copper interface.

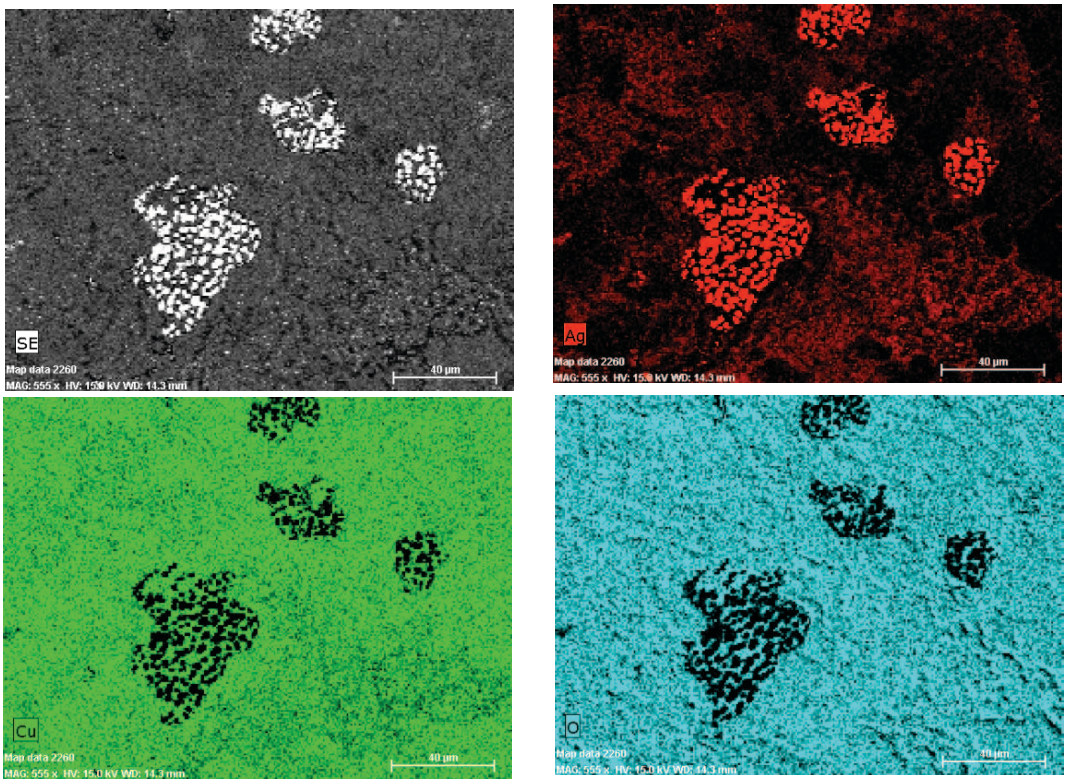

Figure 2.8. EDS compositional maps of Cu-Cu 400°C, 5 MPa, UT ink, sample #1. The bright regions can be seen to be silver while the remaining material consists of a mixture of copper and oxygen, suggesting that the fracture surface is predominately a layer of copper oxide.

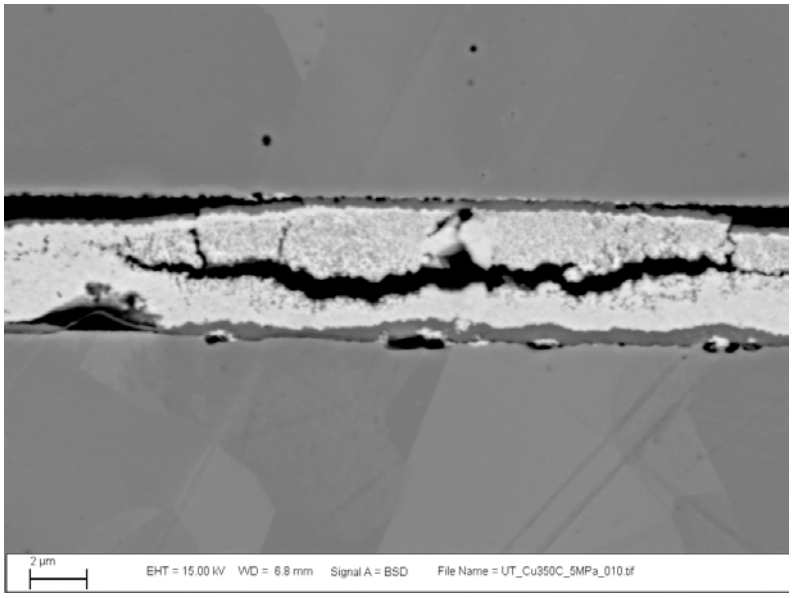

Figure 2.9. Back-scattered electron image of a polished cross-section of untested specimen, Cu-Cu 350°C, 5 MPa, UT ink. Multiple fractures can be seen including copper oxide separated from the substrate along the top left and right edges of the copper and silver bonded regions as well as cracking within the silver layer.

3. Computational Modeling and Simulation

3.1 Introduction

The objective of this work was to determine if joining of Cu-plates by Ag nanoparticles at low temperatures under very modest applied uniaxial stress could be due to sintering. A model for sintering under these conditions was developed by adapting a SPPARKS-based model to simulate microstructural evolution during joining under uniaxial pressure. However, before simulation the effects of applied stress, the magnitude of sintering in these simulations of arbitrary sized-particles had to be determined, as it is necessary to know the relative magnitude of the applied stress to the inherent sintering stress. Thus, two sets of simulations are described. One is simulation of free-sintering and the other under uniaxial pressure.

This document demonstrates the extension of the kMC model to simulate pressure assisted sintering. First, a description of sintering stress and its calculation is included. Second, the implementation of the pressure-assisted sintering is drafted. Then, a preliminary set of results is discussed. Finally, conclusions are drawn and directions of future work are suggested.

3.2 Sintering Stress

The sintering stress, denoted P_L, is defined as the mechanical stress responsible for densification during sintering. The densification rate for the diffusion-controlled mechanisms may be written in general form as [1]:

$$\frac{1}{\rho}\frac{d\rho}{dt} = -\frac{3}{L}\frac{dL}{dt} = \frac{3\phi}{\eta}\left(\sigma_a + P_L\right) \tag{1}$$

Where: ρ stands for relative density; t represents time; $(1/L)dL/dt$ is the linear strain rate, which is equal to 1/3 of the volumetric strain rate; ϕ is the stress intensification factor, η is material viscosity and σ_a is the external applied stress.

The pressure associated with a curved surface is described by the Laplace equation [2]:

$$\sigma = \gamma_{ps}\left(\frac{1}{r_1} + \frac{1}{r_2}\right) \tag{2}$$

Here, σ represents sintering pressure, or sintering potential [1]. The curvature of the surface is specified in terms of the principal radii of curvature for the surface, noted as r_1 an r_2, and the surface energy of the material is represented by γ_{ps}. A flat surface (zero curvature) has zero sintering pressure. A porous body, or any compact formed by loose packed particles, has its own set of curved surfaces storing a corresponding level of stress. Sintering stress and sintering potential are related as:

$$P_L = \frac{\sigma}{\phi} \tag{3}$$

During sintering any surface with a bump or dip will tend to flatten over time to remove the stress [2]. This tendency to minimize the curvature is one of the driving forces behind the sintering phenomena. The sintering stress is a useful measure to quantify this tendency.

In more formal terms, the continuum theory of sintering defines the sintering stress as the derivative of the free energy per unit mass with respect to the volumetric mass of the porous material [4]. This definition provides a procedure to obtain a quantitative measure of sintering stress as:

$$P_L = \frac{1}{\rho}\frac{dF}{d\rho} \tag{4}$$

where: F is the surface free energy and is proportional to the pore surface area. Besides this, the volumetric mass of the porous material is equal to the inverse of the relative density. In summary, to calculate the sintering stress it is enough to compute the evolution of both the pore surface area and the relative density for the system.

Sintering stress is an important measure to characterize the behavior of the sintering system. It quantifies the surface curvature contribution to the sintering driving force. Other factors can contribute to drive the sintering process, for example the application of an external pressure can enhance the densification of porous specimen. The sintering stress, calculated for a system under free sintering, provides a scale to evaluate the relative contribution of these other factors.

3.2.1 Calculation of Sintering Stress

Based on the availability of detailed microstructures for the evolution of the 3D compact, the sintering stress has been calculated following a similar method to the one described in [5]. All the quantities obtained from the microstructure are calculated in a *sample volume*: a volume occupying the core of the 3D specimen. The computations are done in the sample volume to avoid possible artifacts arising from the edge. Although a large number of particles are used in the simulations, compared to real sintering materials, the fraction of particles at the edges of the simulation is very large. These particles shape evolve in a different manner than the interior particle to minimize their surface free energy. Thus the sample volume is restricted to the core with no edge particles.

The process to calculate sintering stress is:

1. Calculation of pore surface. The pore surface is calculated as the average pore sites surrounding each grain site in the test volume. It can be expressed as:

$$S = \frac{\sum_{i=1}^{N}\sum_{j=i}^{n} J_{ij}}{N} \tag{5}$$

where: sub-index i runs over all the sites in the test volume, sub-index j runs over all the neighboring sites of i, n is the total neighbors of site i and N is the total number of sites in the test volume. J takes value of zero if i is a grain site and j, the neighbor site, is also a grain site, i.e. $J_{gg} = 0$; it takes value of one if i is a grain site and j, the neighbor site is a pore site, i.e. $J_{gp} = 1$; and it takes value of zero if i is a pore site, i.e. $J_{pj} = 0$.

2. Calculation of relative density. The relative density is calculated as the ratio of grain sites with respect to the total sites in the test volume. It is equal to:

$$\rho = \frac{N_g}{N} \tag{6}$$

As before, N represents the total sites in the test volume and N_g is the total grain sites in the test volume.

3. Calculation of the derivative of the free energy with respect to the volumetric mass. The derivative is calculated numerically in a three-step procedure.
3.1 A cubic spline is used to fit the raw pore surface vs. relative density data obtained from the microstructure.
3.2 A Chebyshev polynomial approximating the function of pore surface vs. relative density represented by the spline is computed. The computation produces a set of Chebyshev coefficients that completely specify the polynomial and therefore are a synthesis of the pore surface as function of relative density.
3.3 The numerical derivative of the Chebyshev polynomial is easily calculated as an algebraic recurrence operation on the coefficients of the Chebyshev polynomial computed in 3.2.

Chebyshev polynomials approximate a function in a certain range. The approximation is such that among all polynomials of the same degree, the Chebyshev polynomial has the smallest maximum deviation from the true function [6]. To calculate the coefficients representing the Chebyshev polynomial the function to be approximated needs to be evaluated in an arbitrary set of points. A cubic spline interpolation is built in the first place to provide the capacity to evaluate the pore surface at required values of relative density. To guarantee that a reasonable spline interpolation is built a convenient number of data points for pore surface and relative density is computed. The easiness to obtain the numerical derivative for the Chebyshev polynomial completely justifies the extra step incurred. Moreover, the derivative produced in this way is less noisy than results obtained by the numerical derivation of the cubic spline [5].

3.2.3 Pressure-Assisted Sintering

The application of an external stress or pressure to the powder system during sintering is a procedure used to enhance densification in solid-state sintering [1]. The auxiliary external applied stress comes to supplement the small sintering stress. In many cases, the external pressure becomes a dominant term acting to close pores and densify the compact [2].

The densifying mechanisms, as lattice diffusion and grain boundary diffusion, are significantly enhanced by the application of an external pressure [1]. Other mechanisms can also be activated, as particle rearrangement or grain boundary sliding, however these are thought to be minimal or non-existent at the low applied stresses being considered in this work. Also, the dominant mechanisms may change depending on configuration factors as size of particles or composition. It is difficult to assess the impact of those factors. Here a rudimentary procedure to simulate sinter forging is proposed. The modifications introduced are rather simple and reproduce some of the qualitative behavior of the real pressure-assisted sintering. The procedure is described next.

3.2.4 Incorporation of Assisted-Pressure Mechanism into the Sintering kMC Model

The incorporation of an externally applied pressure into the kMC model is accomplished by modifying two of the main mechanisms of the regular sintering simulation, namely the surface diffusion and the densification by annihilation.

- Surface diffusion: Surface diffusion at the particle-pore surface is simulated by exchanging grain sites and pore sites with each other. This exchange mechanism is modified due to the applied uniaxial stress. Surface diffusion is such that porosity diffuses preferentially perpendicular to the direction of applied stress and mass diffuses parallel to the direction of applied stress.

- Modification of Annihilation: The densification algorithm under free sintering conditions simulates the centers of mass of neighboring grains approaching each other. This is done by moving the center of mass of the grains towards the grain boundary where annihilation takes place. However, when an uniaxial stress is applied, the centers of mass are biased to approach each other along the direction of applied stress. The angle between the regular annihilation path and the axis of the externally applied pressure is calculated. If the angle is greater than 35^o the annihilation path is rotated towards the axis of the applied pressure. The angle of rotation is proportional to current deviation and the factor used is the cosine. If the angle is smaller than 35^o then no modification is made and the annihilation proceeds as the regular case. In other words, if μ_r stands for the angle of rotation and μ is the original angle between the regular annihilation path and the axis of the externally applied pressure:

$$\mu_r = \begin{cases} \mu\cos(\mu) & \mu \geq 35^o \\ 0 & \mu < 35^o \end{cases} \tag{7}$$

Again, this modification is introduced to bias the mass movement in a direction perpendicular to the applied stress.

Both modifications are applied if the norm of the applied pressure is greater than the sintering stress calculated for the configuration when free sintering is simulated, i.e. when the pressure applied constitutes the main mechanism driving the sintering process.

3.3 Results

Results for two different configurations of random packing of particles are shown. Regular configurations of spherical, particles are studied. Configuration A is composed by 400 particles with a radius ranging from 0.945 to 1.084 microns, and mean of 1 micron. The initial packing density is 63.6 %. Configuration B is composed of 4000 particles with radius of 0.46 microns and initial packing density of 63.8 %. Figure 3.1 and 3.2 show 3D views and 2D slices of Configurations A and B respectively.

3.3.1 Results for Free Sintering

Configuration A: Figure 3.3 includes 2D slices of microstructure evolution. Figures 3.4, 3.5 and 3.6 show the evolution of different variables. Figure 3.4 depicts the densification curve. Figure 3.5 displays results for sintering stress as a function of relative density. The graph includes 4 plots: (i) the green points represent the pore surface area and relative density calculated from the microstructure evolution, (ii) the red curve displays the cubic spline fit of the raw data, (iii) the blue curve is the Chebyshev polynomial approximating the spline fit and (iv) the purple curve is the sintering stress computed as the numerical derivative of the Chebyshev polynomial approximation. Figure 3.6 plots engineering strains for x, y and z directions.

The sintering stress is initially negative due to surface roughening induced by the finite temperature simulations. But, then it is large when necks grow quickly and stabilizes to a near constant value. The strains are very nearly isotropic with a slightly lower strain in the x-direction. This we attribute to a slight anisotropy in the packing of the spheres in this direction.

Note that the sintering stress is reported as an average over the sample volume. The values shown are dimensionless values. Real units of sintering stress can be obtained multiplying the dimensionless values by the surface energy of the material.

Configuration B: Figure 3.7 includes 2D slices of microstructure evolution, Figure 3.8 plots densification, Figure 3.9 displays sintering stress, including raw data as well as spline and Chebyshev fits, and Figure 3.10 shows engineering strains.

While results are very similar to Configuration A, the densification rate is much higher as expected for the smaller particle size. The sintering stress shows the same trends as Configuration A, but is higher in magnitude. In the region of high density, the porosity becomes closed with isolated pores and the sintering increases with density. The strains in the three directions are identical as packing is completely isotropic in this simulation.

3.3.2 Results for Pressure-Assisted Sintering

A uniaxial pressure in the Z direction is applied to both systems and simulations are computed using the same set of parameters. The pressure applied is the same for both configurations and is roughly equivalent to double the sintering stress, taken as the mean value at the end of the sintering stress plot for Configuration B (Figure 3.9).

Configuration A: Figure 3.11 displays 2D slices of microstructure evolution, Figure 3.12 densification and Figure 3.13 engineering strains. The microstructure is clearly anisotropic with elongated pores and particles. The strain is large in the direction of applied stress and virtually nil in the other directions. This reflects the fact that, in this case, the driving force for sintering seems to be dominated by the contribution of the external applied stress with just a marginal effect from the sintering stress. In addition, the densification rate is higher than that for the no-applied-stress case. This is also as expected since the total driving force for densification is higher.

Configuration B: Figure 3.14 displays 2D slices of microstructure evolution, Figure 3.15 densification and Figure 3.16 engineering strains. Again qualitatively the results are similar to

Configuration A, however, the densification rate is much higher and the strains in the direction of applied stress are higher. Furthermore, the strains in the other two directions are also higher. This we attribute to the higher inherent sintering stress of the smaller particles.

3.4 Conclusions

1. A preliminary procedure to incorporate pressure-assisted sintering into the kMC model is described. Results are encouraging because most of the qualitative behavior observed in real systems is reproduced. This indicates that sintering theory and simulation can be useful for understanding NEDB.

2. Densification is enhanced by an applied uniaxial stress, in agreement with experimental observations on NEDB bonds.

3. The compact is deformed in accordance with the stress applied. Grains as well as pores elongate in the direction perpendicular to the applied pressure. Strains calculated serve as a direct measure of the anisotropy of deformation caused by the external stress.

4. The value of the sintering stress is higher for the set of smaller particles (Configuration B), as expected from NEDB results.

5. As future work it is worth to study the effect of changing some controlling parameters in the pressure-assisted annihilation. Different grades of deformation can be obtained by varying the threshold angle to modify the annihilation path or the multiplicative factor in the angle of rotation. Those parameters should depend on the material or composite simulated and on external conditions as temperature and pressure level. Also, it could be interesting to devise analogous modification to simulate isostatic pressing.

3.5 References for Section 3

1. M. N. Rahaman, “Sintering of Ceramics”, CRC Press, 2008.
2. R. M. German, *Sintering Theory and Practice*, John Wiley & Sons, 1996.
3. V. Tikare, M. V. Braginsky, D. Bouvard and A. Vagnon, “An experimental validation of a 3D kinetic Monte Carlo model for microstructural evolution during sintering”, *Advances in Science and Technology*, vol. 45, pp. 522—529, 2006.
4. E. A. Olevsky, "Theory of sintering: from discrete to continuum", *Materials Science and Engineering*, vol. R23, pp. 41—100, 1998.
5. E. Olevsky, V. Tikare and T. Garino, "Multi-Scale Study of Sintering: A Review", *J. Am. Ceram. Soc*., vol. 89 (6), pp. 1914 – 1922, 2006.
6. W. H. Press, S. A. Teukolsky , W. T. Vetterling and B. P. Flannery, *Numerical Recipes in C: The Art of Scientific Computing*, Cambridge University Press, 2nd Ed., 1992.

3.6 Figures for Section 3

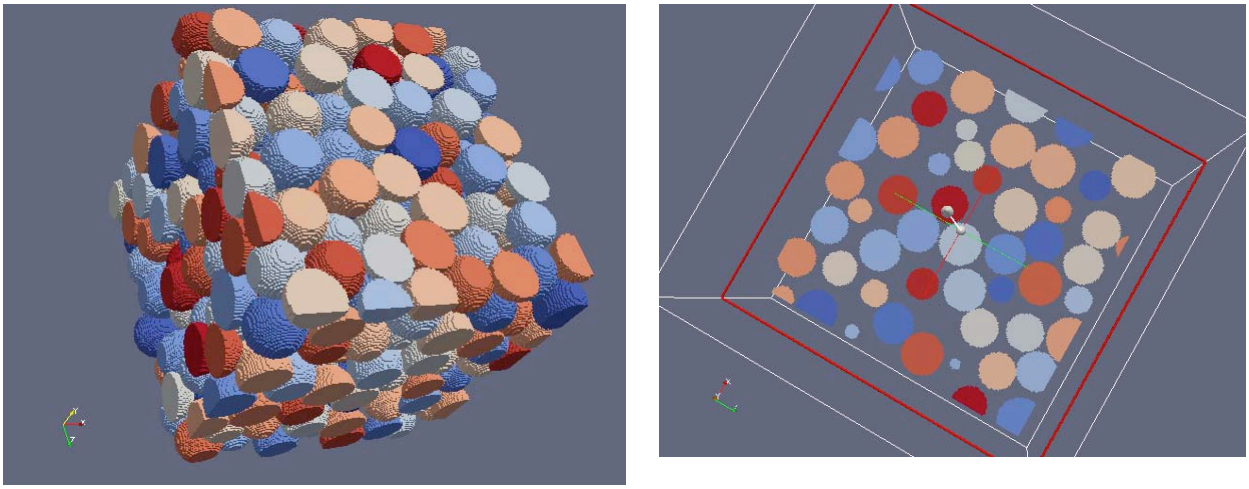

Figure 3.1. Configuration A: 400 Particles – Initial State. Left: 3D view. Right: 2D slice.

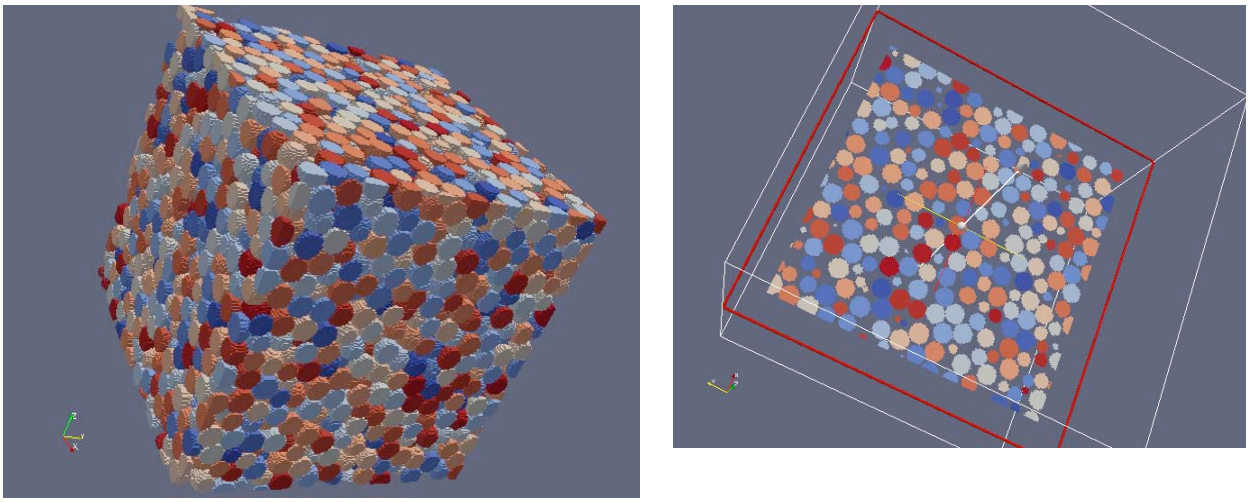

Figure 3.2. Configuration B: 4000 Particles – Initial State. Top: 3D view, Bottom: 2D slice.

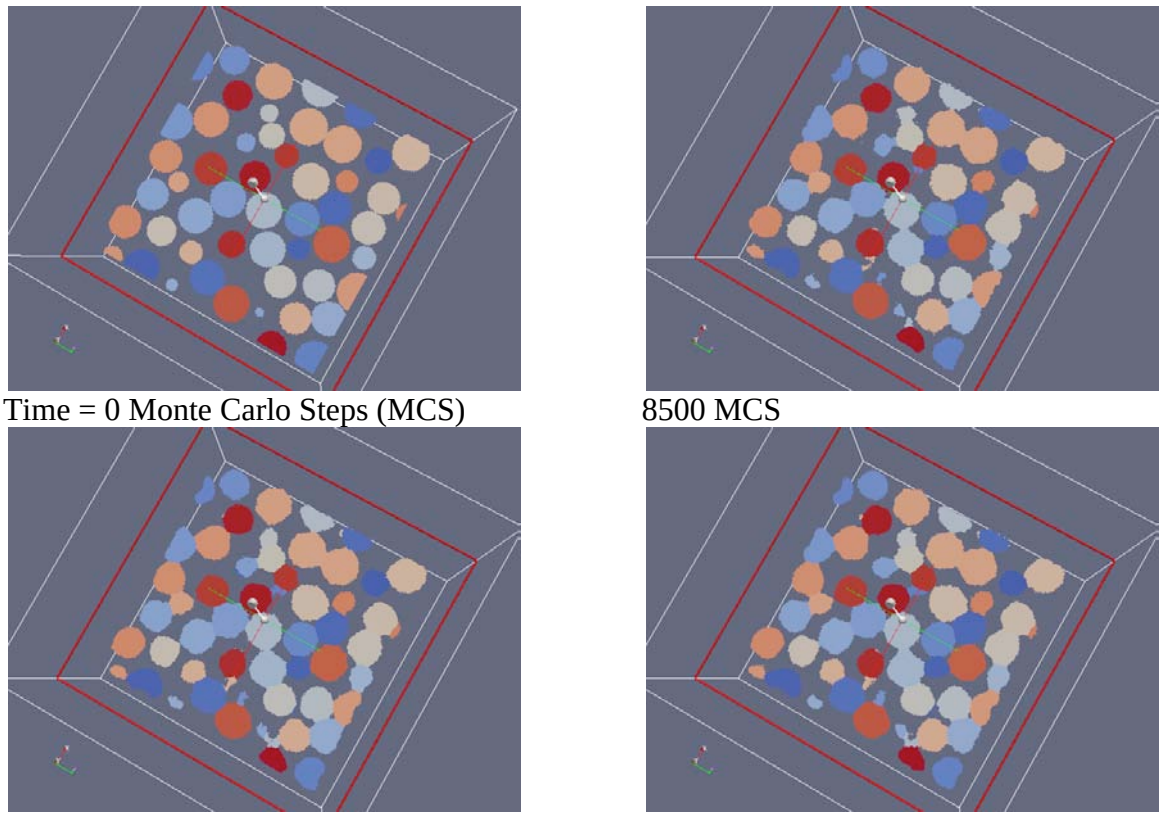

Figure 3.3. Configuration A – Free Sintering – 2D slices of microstructure evolution.

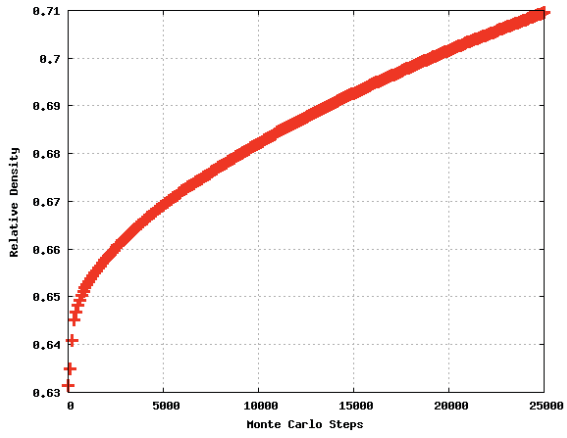

Figure 3.4. Configuration A – Free Sintering – Densification.

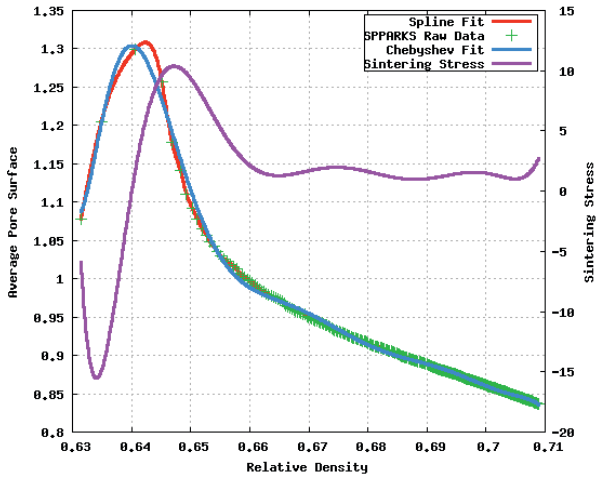

Figure 3.5. Configuration A – Free Sintering – Sintering Stress.

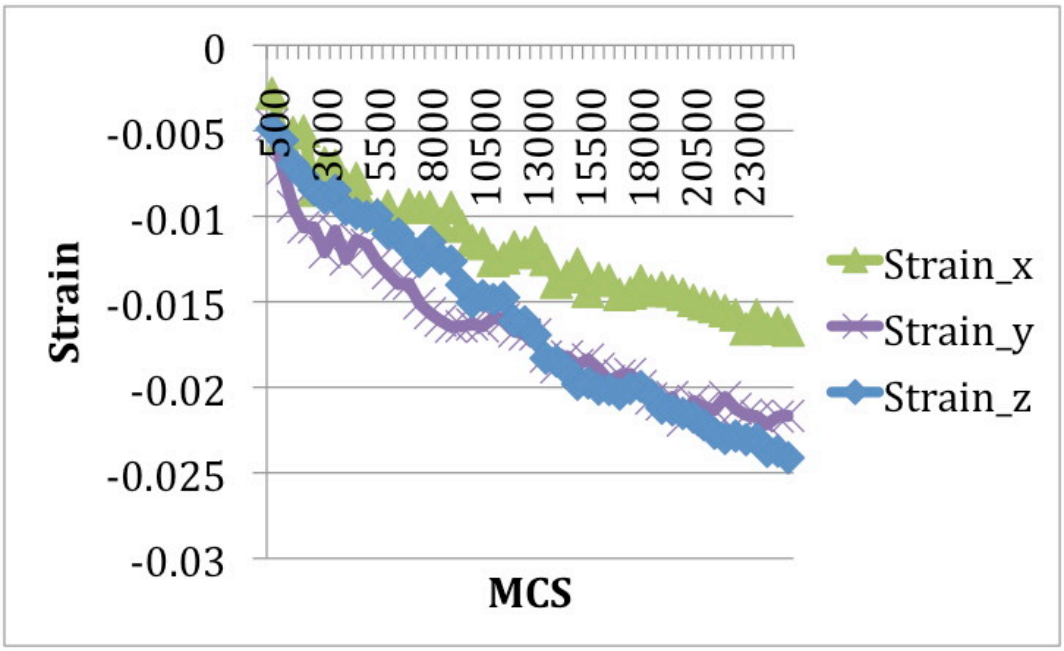

Figure 3.6. Configuration A – Free Sintering – Engineering Strains.

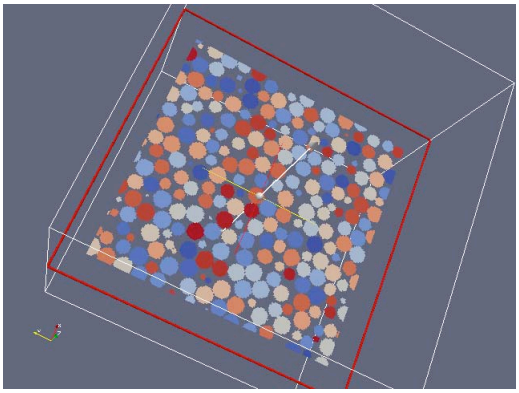

Time = 0 Monte Carlo Steps (MCS)

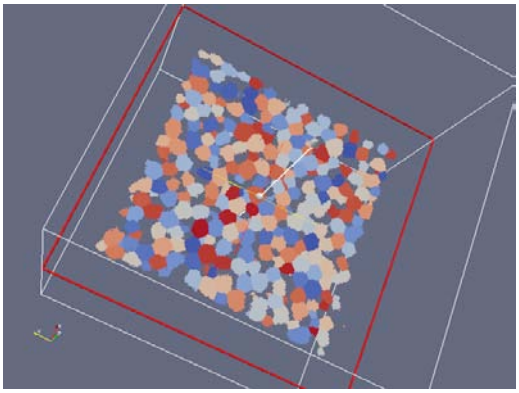

10,000 MCS

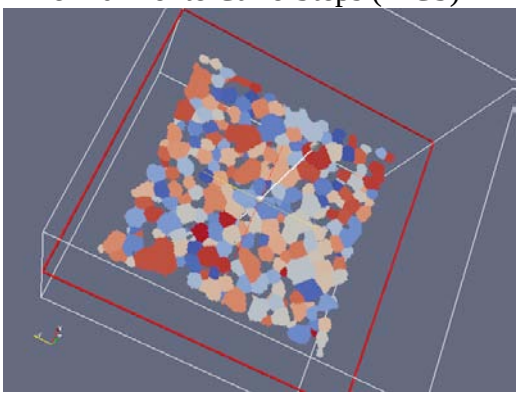

20,000 MCS

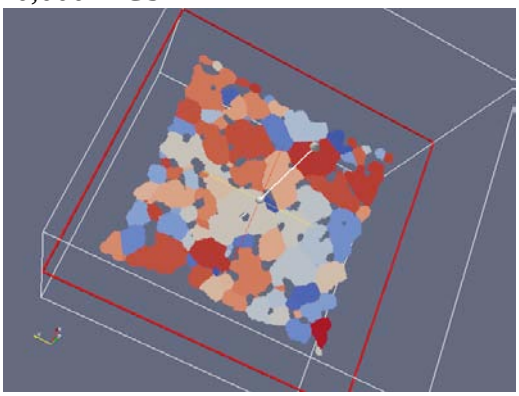

30,000 MCS

Figure 3.7. Configuration B – Free Sintering - 2D slices of microstructure evolution.

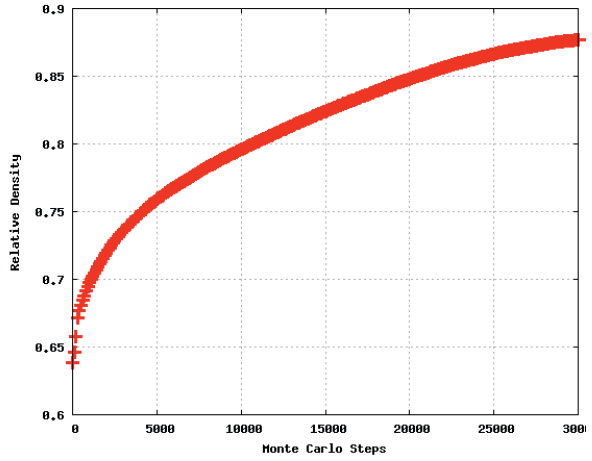

Figure 3.8. Configuration B – Free Sintering – Densification.

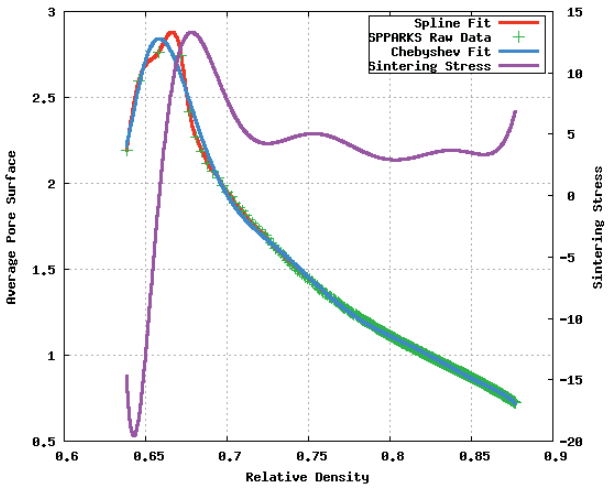

Figure 3.9. Configuration B – Free Sintering – Sintering Stress.

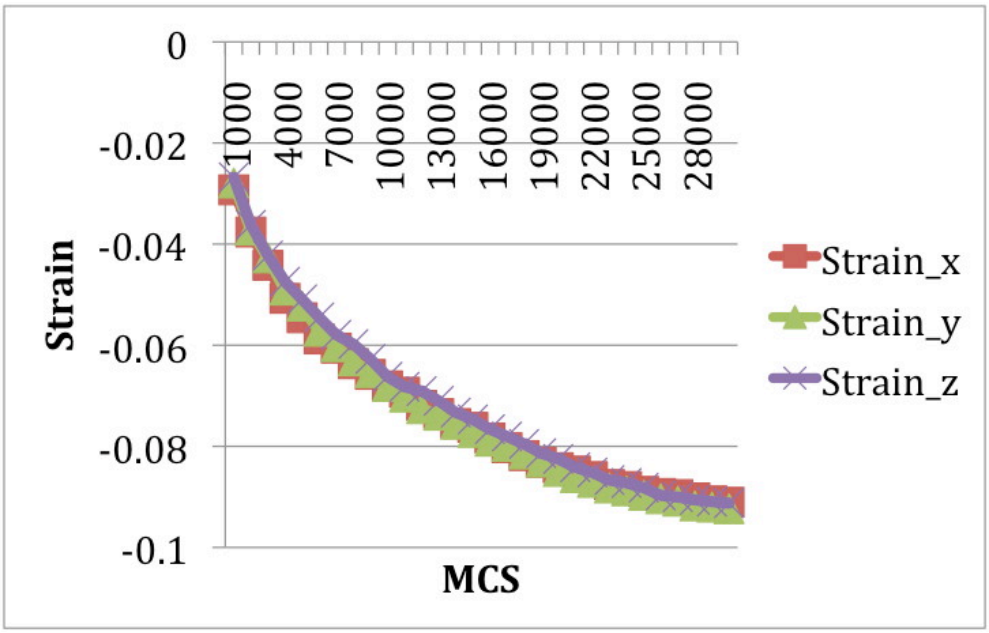

Figure 3.10. Configuration B – Free Sintering – Engineering Strains.

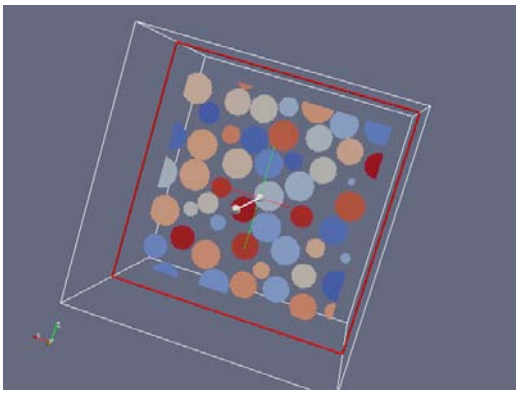

Time = 0 Monte Carlo Steps (MCS)

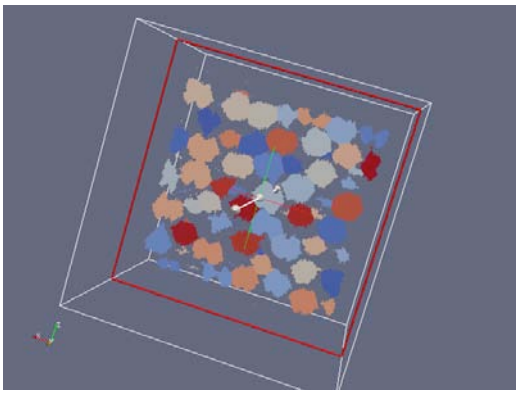

8500 MCS

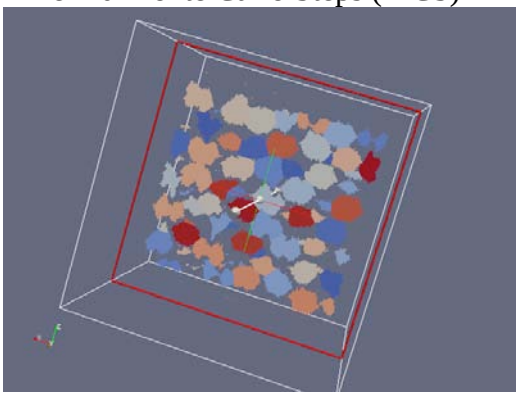

17,000 MCS

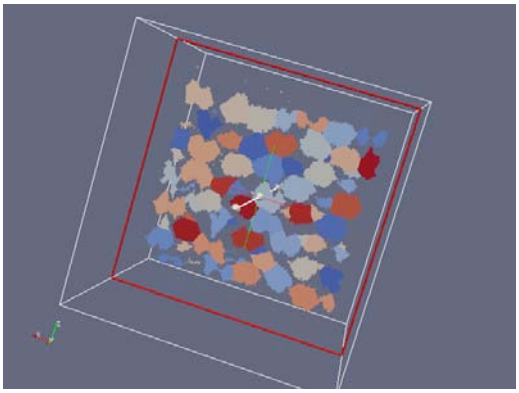

25,000 MCS

Figure 3.11. Configuration A – Pressure-Assisted Sintering – 2D slices of microstructure evolution. Applied pressure is parallel to the Z axis, almost vertical in these graphs.

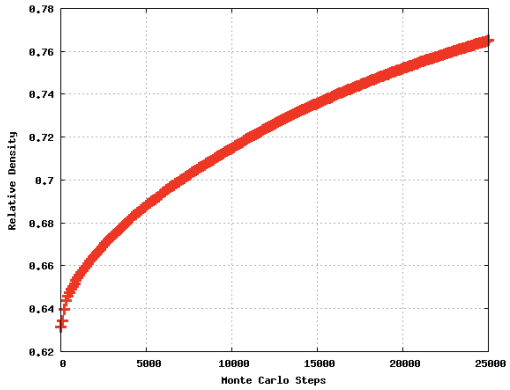

Figure 3.12. Configuration A – Pressure-Assisted Sintering – Densification.

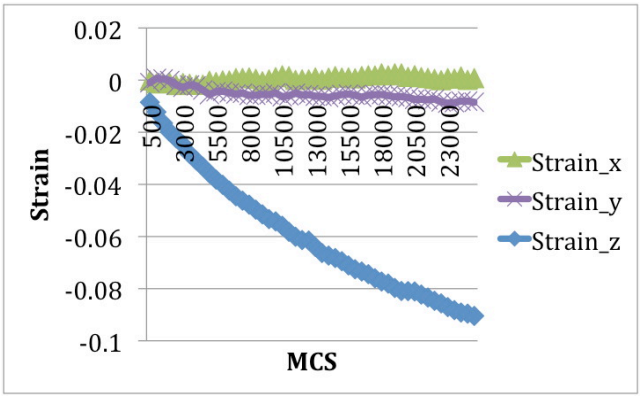

Figure 3.13. Configuration A – Pressure-Assisted Sintering – Engineering Strains.

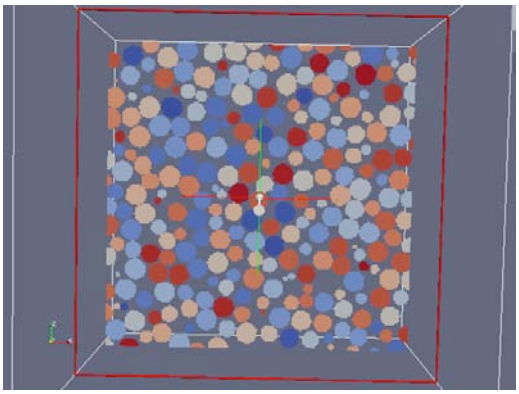

Time = 0 Monte Carlo Steps (MCS)

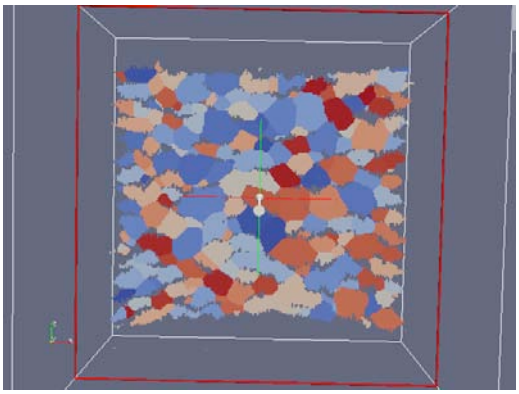

10,000 MCS

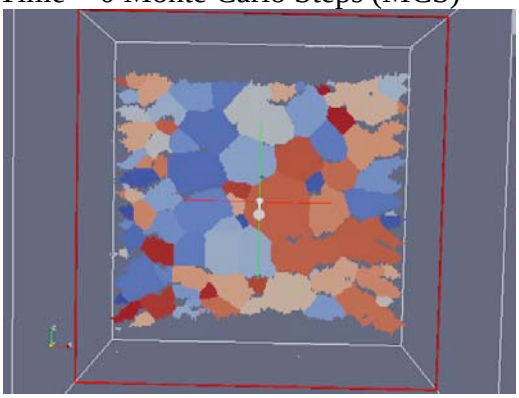

20,000 MCS

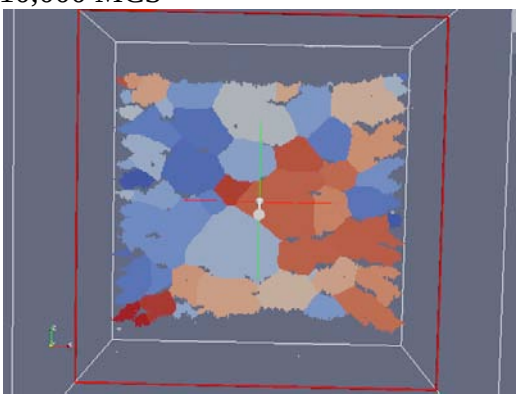

30,000 MCS

Figure 3.14 – Configuration B – Pressure-Assisted Sintering – 2D slices of microstructure evolution. Applied pressure is parallel to the Z axis, almost vertical in these graphs.

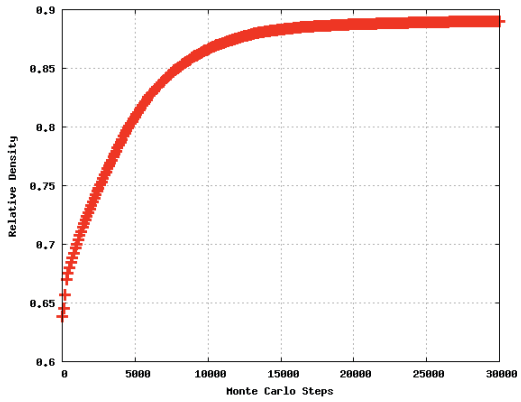

Figure 3.15. Configuration B – Pressure-Assisted Sintering – Densification.

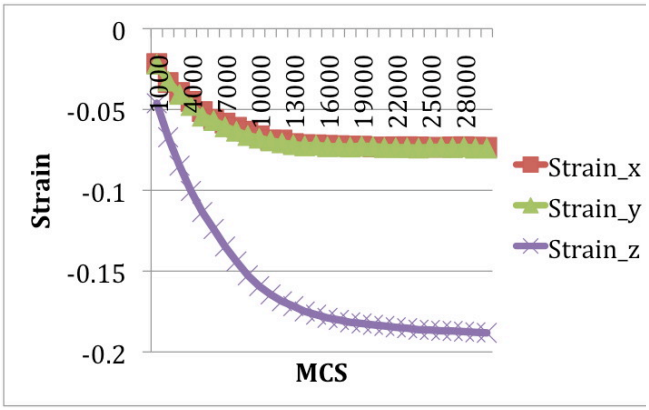

Figure 3.16. Configuration B – Pressure-Assisted Sintering – Engineering Strains.

DISTRIBUTION:

1	electronic	Donna Chavez, LDRD Office	1911
1	electronic	Elizabeth Holm	1814
1	electronic	R. Allen Roach	1814
1	electronic	James Aubert	1822
1	electronic	Joseph Puskar	1822
1	electronic	F. Michael Hosking	1831
1	electronic	Mark Reece	1831
1	electronic	Ken Sorenson	6774
1	electronic	Veena Tikare	6774
1	electronic	Technical Library	9536
1	electronic	Cristina Garcia Cardona	SDSU
1	electronic	Luke Brewer	NPS


Sandia National Laboratories